Out-of-equilibrium charge dynamics in a hybrid circuit quantum electrodynamics architecture

J. J. Viennot, M. R. Delbecq, M. C. Dartiailh, A. Cottet, and T. Kontos*
Laboratoire Pierre Aigrain, Ecole Normale Supérieure, CNRS UMR 8551, Laboratoire associé aux universités Pierre et Marie Curie et Denis Diderot, 24, rue Lhomond, 75231 Paris Cedex 05, France
(Received 13 December 2013; revised manuscript received 14 March 2014; published 4 April 2014)

The recent development of hybrid circuit quantum electrodynamics allows one to study how cavity photons interact with a system driven out of equilibrium by fermionic reservoirs. We study here one of the simplest combination: a double quantum dot coupled to a single mode of the electromagnetic field. We are able to couple resonantly the charge levels of a carbon-nanotube-based double dot to cavity photons. We perform a microwave readout of the charge states of this system, which allows us to unveil features of the out-of-equilibrium charge dynamics, otherwise invisible in the DC current. We extract the relaxation rate, dephasing rate, and photon number of the hybrid system using a theory based on a master equation technique. These findings open the path for manipulating other degrees of freedom, e.g., the spin and/or the valley in nanotube-based double dots using microwave light.

DOI: 10.1103/PhysRevB.89.165404 PACS number(s): 73.23.−b, 73.63.Fg

Confined electronic states in quantum dot circuits allow to encode and manipulate quantum information. Double quantum dot structures are particularly appealing in that context because they can be described with a simple Hilbert space, yet providing the necessary control for quantum manipulation of spin or charge degrees of freedom [1]. Recently, on-chip photonic cavities coupled to the charge of double quantum dots have appeared as a promising new toggle for manipulating quantum information [2–5]. Such a hybrid circuit quantum electrodynamics (cQED) architecture can be used to readout single quantum dots [6] and to couple distant quantum dot circuits [7]. It could also be used to couple coherently distant spins and read them out in a quantum nondemolition manner [8], provided the strong spin/photon coupling is achieved. The strong spin/photon coupling requires a large spin photon coupling strength and long spin dephasing times. Both theses features remain to be observed in the double dots cQED structures demonstrated so far.

Single wall carbon nanotubes are interesting in that context because they provide, in contrast to the other platforms based on InAs nanowires or GaAs/AlGaAs two-dimensional electron gas, a nuclear spin free environment if grown with isotopically pure ^{12}C. Furthermore, they can easily be coupled to various kinds of electrodes, which could lead to new spin manipulation schemes [9–14].

In this paper, we demonstrate that we can embed nanotube-based double quantum dots into high-quality factor microwave cavities. We demonstrate that these devices behave like an effective spin which can be brought into resonance with the cavity photons. We use the cavity to readout this effective spin in out-of-equilibrium conditions when a large power is applied to the cavity or a finite bias is applied to the double quantum dot (DQD). Finally, we are able to observe the microwave spectroscopy of the charge levels using a two-tone drive scheme. This method could be easily generalized to characterize other types of degrees of freedom, e.g., the spin and/or the valley [15].

The devices are fabricated using a novel stamping technique [16] that allows us to combine highly isolated nanotube-based double quantum dot devices and high-quality factor microwave cavities, adapted from Refs. [17–19]. The nanotube device is fabricated using standard lithography techniques in two steps. The top gates are fabricated using three oxidations/evaporation of 2−nm thick Al layers under an O_2 pressure of 1 mbar for 10 min. The top gates are subsequently covered by 30 nm of Al and 10 nm of Pd. The second lithography step allows us to fabricate the source and the drain electrodes which are 30−nm thick PdNi electrodes [see Fig. 1(d)]. The third step is the fabrication of the microwave cavity using photolithography which allows us to make 100−nm thick Al superconducting microwave resonators. The novel stamping technique is essential here for obtaining reliably quality factors larger than 1000. We think that it is also essential for getting double quantum dot devices with an internal hopping strength comparable with the cavity frequency, which is very difficult in nanotube-based quantum dots. The device presented in the present paper had a quality factor of about 3500 (even for a photon number smaller than 1). The transmission amplitude and phase close to the resonance frequency is shown in Fig. 1(f). Note the hammer finger starting from one of the topgates of the nanotube which is made to increase the asymmetry between the electron-photon couplings to the right and left dots. The resulting device is shown in Figs. 1(b), 1(c), and 1(d). In each of our cavities, we embed two double-dot circuits that could be used to explore nonlocal transport properties mediated by photons in such devices [7,20–23]. The microwave setup used to measure the microwave response of the cavity is essentially similar to the one used by the authors of Ref. [6], but with a cryogenic amplifier stage with a noise temperature of about 5 K. All the microwave measurements are performed at a frequency of 6.72 GHz and at a temperature of 20 mK (electronic temperature about 40 mK).

The natural state basis for the DQD is the molecular state basis of the bonding and antibonding states $\{|B\rangle, |AB\rangle\}$, respectively. We define $\sigma_z = |AB\rangle\langle AB| - |B\rangle\langle B|$. Such a system is a charge quantum bit that is naturally coupled to the microwave photons of the cavity. Provided the coupling between the photons and the two dots is asymmetric, one can

*To whom correspondence should be addressed: kontos@lpa.ens.fr

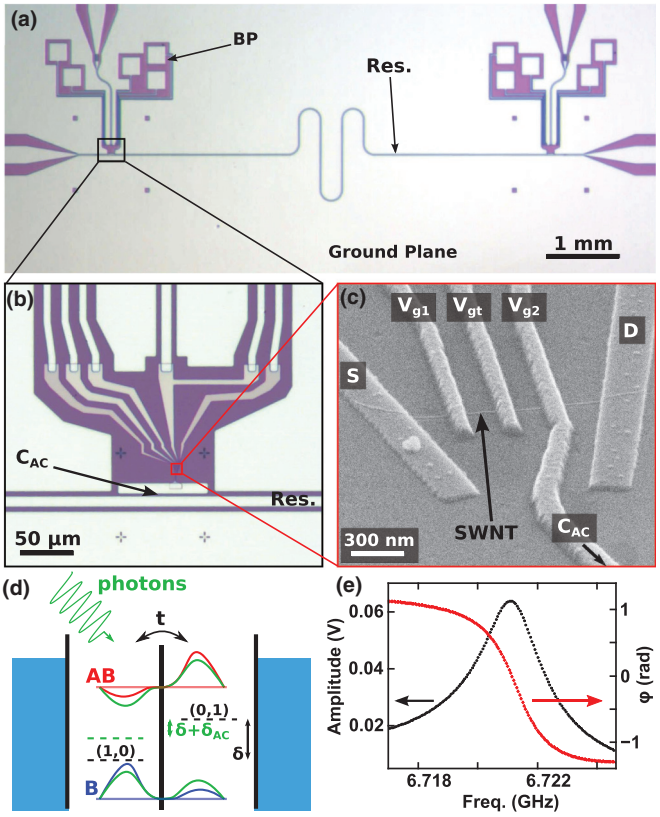

FIG. 1. (Color online) (a) Optical micrograph of the coplanar wave-guide microwave resonator (Res.). Bonding pads (BP) are isolated from the ground plane and carry DC voltage or current. (b) An extra superconducting pad is placed next to the resonator line, providing a large capacitance C_{AC}. (c) Scanning electron micrograph of the double quantum dot device. A single wall carbon nanotube (SWNT) is connected to source and drain electrodes (S and D), as well as three top gates (V_{g1}, V_{g2}, and V_{gt}). V_{g2} is directly connected to the capacitance C_{AC}. (d) Schematic of the coupling mechanism between the microwave photons and bonding (B) and antibonding (AB) states of the double quantum dot. (e) Amplitude and phase response of the microwave cavity in its fundamental mode measured in transmission.

map the Hamiltonian of the system onto a Jaynes-Cummings Hamiltonian of the pseudospin coupled to the cavity [2,3,14]. We assume that we drive the cavity with a classical field of pulsation ω_d. Solving the coupled dynamics of the spin-photon system with a semiclassical decoupling of the photonic and electronic degrees of freedom [24], we obtain the following dispersive shift for the cavity photons:

$$\Delta f = \mathrm{Re}[\chi]\langle\sigma_z\rangle, \tag{1}$$

where $\chi = \frac{(g_0 \sin\theta)^2}{-i(\gamma/2+\Gamma_\phi)+\Delta}$ is the susceptibility of the system. The parameters entering in χ are the charge-photon coupling strength g_0, the hybridization angle θ, the qubit-microwave drive detuning $\Delta = \Omega - \omega_d$, the energy difference between the bonding and antibonding states Ω, the effective spin relaxation and dephasing rates γ and Γ_ϕ, respectively.

As shown in Fig. 2, the phase is finite only at the degeneracy lines between (N,M) and $(N-1,M+1)$ charges states, which is highlighted by a dashed line between the two triple

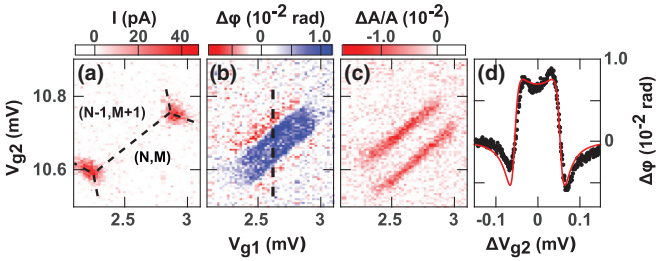

FIG. 2. (Color online) (a) Direct current flowing trough the device measured at $V_{sd} = 20\,\mu$V as a function of V_{g1} and V_{g2}, with $V_{gt} = -242$ mV. The dashed lines outline the stability diagram of charge states (N,M). (b) Phase variation of the transmitted microwave signal measured at cavity resonance ($\simeq 6.72$ GHz), simultaneously with the direct current of (a). The associated charge susceptibility appears at degeneracy between (N,M) and $(N-1,M+1)$. (c) The amplitude variation $\Delta A/A$ of the microwave signal exhibits two parallel lines corresponding to the regions where the bonding/antibonding frequency energy splitting equals the cavity frequency. (d) Microwave phase variation (black points) measured along the dashed line of (d). Solid red line is theory described in the main text.

points visible in the DC current in Fig. 2(a). Such a phase contrast shows that photons couple mainly asymmetrically to the two dots and induce transitions from the left (L) to the right (R) dot and vice versa in this gate region [25,26]. In Fig. 2(d), the peak with lateral satellite dips of the phase show that the B/AB doublet becomes resonant with the cavity when the phase changes sign. The red line in Fig. 2(f) fits this phase contrast with Eq. (1) and $\langle\sigma_z\rangle = -1$. It allows us to get $g_0 = 3.3$ MHz, $\gamma/2 + \Gamma_\phi = 550$ MHz, and $2t = 5.5$ GHz. Depending on the setting of the three gates, we get values for g_0 and $\gamma/2 + \Gamma_\phi$ ranging from 3 to 12 MHz and from 450 to 3 GHz, respectively. These figures are comparable to what is found in two dimensional electron gas (2DEGs) [2,4] and in InAs nanowires [3]. The nonlinear photonic and/or electronic regimes that have not been investigated so far allow one to get a deeper understanding of the double-dot/cavity hybrid system.

We now turn to the finite bias regime in the low power limit. Figure 3 displays the DC current and the cavity response for finite bias $V_{sd} = -350, 50,$ and $250\,\mu$V. This leads to characteristic transport triangles in the transport spectroscopy. These triangles indicate that the populations of the ground and first excited states are strongly out of equilibrium, leading to $\langle\sigma_z\rangle$, which now only depends on the internal relaxation rate and the coupling to the leads. As shown in Fig. 3, the phase contrast remains essentially identical at $50\,\mu$V and in the linear regime of Fig. 2(b), with a B/AB degeneracy line spanning between the two triple points of the double dot. At $250\,\mu$V, the degeneracy line shrinks with weak phase contrast under the top red triangle and a finite residual contrast under the bottom red triangle. This means that $\langle\sigma_z\rangle$ is strongly reduced under the top triangle (equal population for the bonding and antibonding states), whereas it stays finite (negative) under the bottom triangle. This shows the interest of the microwave phase signal in this out-of-equilibrium situation. The top and bottom triangles are nearly identical and have similar current contrast, whereas the phase contrast is markedly different because it directly reveals the value of $\langle\sigma_z\rangle$. For opposite bias

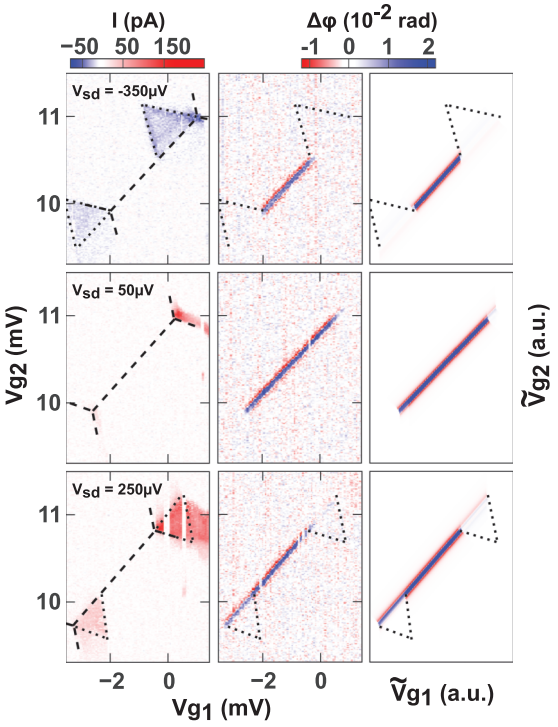

FIG. 3. (Color online) Measured direct current (first column), measured microwave phase (second column), and theory for microwave phase (third column) of the device at three different biases, as a function of gate voltages V_{g1} and V_{g2} ($V_{gt} = -242$ mV). Big dashed lines outline the charge stability diagram of the double quantum dot. The direct current signal shows the characteristic bias triangles (marked with small dashed lines) developing next to the triple points. The phase signal is unchanged between the bias triangles, where the charge remains blockaded, whereas it is modified in the regions where transport is allowed.

as illustrated in the top panel of Fig. 3 ($V_{sd} = -350\,\mu$V), $\langle\sigma_z\rangle$ goes to zero under both triangles. This signals asymmetric coupling to the DQD leads. As shown in the rightmost panels of Fig. 3, we are able to reproduce the observed features with our theory [24]. Reproducing the features of the phase strongly constraints the bare lead couplings to $\gamma_{L(R)} \approx 300(1600)$ MHz for $V_{sd} > 0$ and $\approx$10(10) GHz for $V_{sd} < 0$, respectively. The latter large values probably signal that cotunneling contributes for this bias, although it is not visible in the current. The internal relaxation rate is also constrained to about 300 MHz.

The power dependence of the phase contrast at zero detuning allows one to determine the ratio between the relaxation rate and the cavity photon number at a given power. As depicted in Fig. 4(a) in the inset, photons exert a transverse torque on average on the charge qubit effective spin towards the equatorial plane of the Bloch sphere, thereby reducing the value of $\langle\sigma_z\rangle$. Since the photons *drive* the effective spin, the efficiency of this process is directly related to the relaxation rate of the effective spin. Our theory allows to fit quantitatively our data using the above estimate of $\gamma \approx$ 300 MHz. Specifically, the fit with the red solid line of Fig. 4(a) corresponds to $\gamma/n_0 = 8.1$ MHz, n_0 being the number of photons in the cavity for an input power of -104 dBm. Using

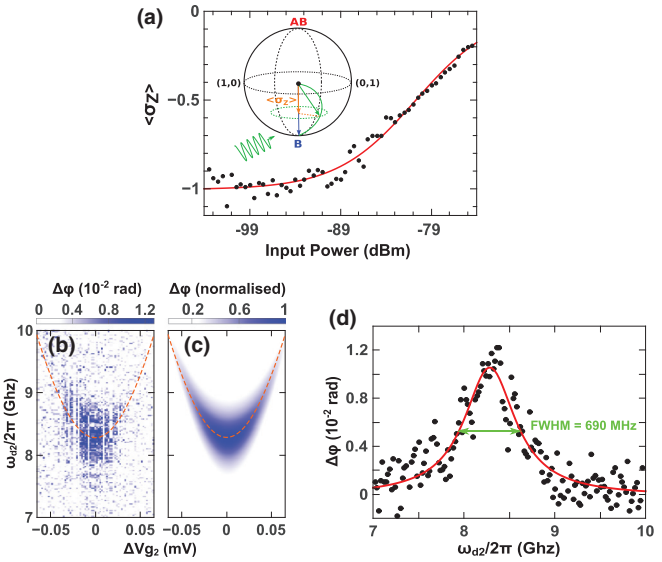

FIG. 4. (Color online) (a) Measured $\langle\sigma_z\rangle$ value (black points) obtained from the phase variation as a function of the estimated microwave power at the input of the cavity. Red line is theory. Inset: Bloch sphere of the charge qbit with bonding and antibonding sates. A large number of photons weakly detuned from the qubit excites transitions and imposes $\langle\sigma_z\rangle > -1$. (b) Two-tone spectroscopy measurement as a function of the double dot detuning and the second-tone frequency $\omega_{d2}/2\pi$. (c) Corresponding simulation using formula (2) in the main text. The phase contrast has been normalized to the maximum. (d) Vertical cut at zero detuning of the two-tone spectroscopy measurement (black circles). The Lorentzian fit in red solid line gives a full width at half maximum (FWHM) of 690 MHz, which is a direct measurement of $\gamma/2 + \Gamma_\phi$.

the estimate of $\gamma \approx 300$ MHz, we find $n_0 \approx 40$ by fitting our data to the theory.

A microwave spectroscopy of the double dot can be performed by measuring the phase contrast at the cavity frequency while exciting the DQD with a second coherent field tone that one can bring in resonance with the bonding/antibonding doublet energy. This is conveniently done when the cavity and the DQD are not in resonance ($2t - \omega_0 > \gamma/2 + \Gamma_\phi$). Defining ω_{d2} the second microwave drive and $n_{\rm drive} = \alpha^2\epsilon_{d2}^2$, the overall dispersive shift reads

$$\Delta f = \mathrm{Re}[\chi]\frac{-1}{1 + \frac{4g^2 n_{\rm drive}}{\gamma}\frac{(\gamma/2+\Gamma_\phi)}{(\gamma/2+\Gamma_\phi)^2+\Delta_2^2}}, \qquad (2)$$

with $g = g_0 \sin\theta$, $\mathrm{Re}[\chi] = g^2\Delta_0/[(\gamma/2 + \Gamma_\phi)^2 + \Delta_0^2]$, $\Delta_0 = \Omega - \omega_0$, and $\Delta_2 = \Omega - \omega_{d2}$. The parameter α is a coupling constant between the second tone drive amplitude ϵ_{d2} that depends on whether the second tone is applied through the input port of the cavity or on a side port directly to a gate on the double quantum dot. We have used both methods and they give similar results. In Fig. 4(b), we present such a measurement. We observe a spot in the detuning-second tone frequency plane around 8 GHz, which is spreading around the zero detuning point. As highlighted by the dashed lines corresponding to the expected resonance frequency, this spot follows roughly the expected dispersion of the charge doublet. In Fig. 4(c), we present the result of the modeling according to formula (2), in

good agreement with the experimental map. As one can see from formula (2), such a measurement allows us to directly access $\gamma/2+\Gamma_\phi$ [which appears naturally in the denominator of formula (2) when the drive amplitude is sufficiently low: $\frac{4g^2 n_{\rm drive}}{\gamma}\frac{(\gamma/2+\Gamma_\phi)}{(\gamma/2+\Gamma_\phi)^2+\Delta_2^2} \ll 1$]. We have checked that we were indeed in this regime for the measurements presented in Fig. 4. A cut of the measurement at zero detuning is presented in Fig. 4(d). We observe a resonance centered around ≈8 GHz with a large amplitude of about 1.2×10^{-2} rad. We can fit the data with the Lorentzian line shape shown in the red line in Fig. 4(d), which is obtained from Eq. (2) (the large amplitude observed is, however, not fully understood). The full width at half maximum (FWHM) of about 690 MHz allows us to get $\gamma/2+\Gamma_\phi \approx 345$ MHz, which is a bit lower than with the previous estimate of 450 MHz. The latter fact is consistent with the $1/2t$ scaling law predicted by the simple dephasing model (see below) since $2t$ is slightly higher here than in the previous sections (slightly different gate set).

The estimates made for γ allow us to determine $\Gamma_\phi \approx$ 300 MHz for the gate setting presented in detail in this paper and $\Gamma_\phi = 3$ GHz for another resonant region (not shown). Our lowest value reported is almost an order of magnitude lower than those reported in Refs. [2,3]. These figures are very important for the future development of devices exploiting other degrees of freedom than the charge, like spin or valley, in carbon nanotubes. They allow us to give an upper bound of the typical charge noise in our device. Indeed, the magnitude of the dephasing rate Γ_ϕ is likely to be due to $1/f$ charge noise in the environment of the nanotube. Using a simple semiclassical model for dephasing at second order in the charge fluctuation [27,28] (at zero detuning, the system is insensitive to charge noise at first order), we can make a link between the extracted $\Gamma'_\phi s$ and the power spectral density of charge noise. If the power spectral density is of the form $\langle\sigma_\epsilon\rangle^2/f$, the dephasing rate Γ_ϕ is expected to be $\approx\frac{d^2\Omega}{d\epsilon^2}\langle\sigma_\epsilon\rangle^2 = \langle\sigma_\epsilon\rangle^2/2t$. Using $2t = 5.5$ GHz we get typically $\langle\sigma_\epsilon\rangle = 5\,\mu$eV when $V_{gt} = -242$ mV, which corresponds to a charge noise of $5\times10^{-4}e/\sqrt{\rm Hz}$. Generally, this allows us to give an upper bound for the charge noise in our device of $5-15\times10^{-4}e/\sqrt{\rm Hz}$. This value compares favorably to the record value [29] reported in GaAs two-dimensional electron gas ($2\times10^{-4}e/\sqrt{\rm Hz}$) and is an important figure of merit for future carbon-nanotube-based quantum information devices [10,14,15].

We acknowledge discussions with B. Huard, F. Mallet, E. Flurin, and P. Campagne. This work was financed by the EU-FP7 Project No. SE2ND[271554] and the ERC Starting grant CirQys.

[1] R. Hanson, L. P. Kouwenhoven, J. R. Petta, S. Tarucha, and L. M. K. Vandersypen, Rev. Mod. Phys. **79**, 1217 (2007).
[2] T. Frey, P. J. Leek, M. Beck, A. Blais, T. Ihn, K. Ensslin, and A. Wallraff, Phys. Rev. Lett. **108**, 046807 (2012).
[3] K. D. Petersson, L. W. McFaul, M. D. Schroer, M. Jung, J. M. Taylor, A. A. Houck, and J. R. Petta, Nature (London) **490**, 380 (2012).
[4] H. Toida, T. Nakajima, and S. Komiyama, Phys. Rev. Lett. **110**, 066802 (2013).
[5] J. Basset, D. D. Jarausch, A. Stockklauser, T. Frey, C. Reichl, W. Wegscheider, T. M. Ihn, K. Ensslin, and A. Wallraff, Phys. Rev. B **88**, 125312 (2013).
[6] M. R. Delbecq, V. Schmitt, F. Parmentier, N. Roch, J. J. Viennot, G. Fève, B. Huard, C. Mora, A. Cottet, and T. Kontos, Phys. Rev. Lett. **107**, 256804 (2011).
[7] M. R. Delbecq, L. E. Bruhat, J. J. Viennot, S. Datta, A. Cottet, and T. Kontos, Nat. Comm. **4**, 1400 (2013).
[8] J.-M. Raimond, M. Brune, and S. Haroche, Rev. Mod. Phys. **73**, 565 (2001).
[9] M. Trif, V. N. Golovach, and D. Loss Phys. Rev. B **77**, 045434 (2008).
[10] A. Cottet and T. Kontos, Phys. Rev. Lett. **105**, 160502 (2010).
[11] X. Hu, Y.-X. Liu, and F. Nori, Phys. Rev. B **86**, 035314 (2012).
[12] A. Cottet, T. Kontos, and A. L. Yeyati, Phys. Rev. Lett. **108**, 166803 (2012).
[13] J. Skoldberg, T. Löfwander, V. S. Shumeiko, and M. Fogelström, Phys. Rev. Lett. **101**, 087002 (2008).
[14] P. Q. Jin, M. Marthaler, A. Shnirman, and G. Schon, Phys. Rev. Lett. **108**, 190506 (2012).
[15] E. A. Laird, F. Pei, and L. P. Kouwenhoven, Nat. Nanotech. **8**, 565 (2013).
[16] J. J. Viennot, J. Palomo, and T. Kontos, Appl. Phys. Lett. **104**, 113108 (2014).
[17] F. Pei, E. A. Laird, G. A. Steele, and L. P. Kouwenhoven, Nat. Nanotech. **7**, 630 (2012).
[18] C. C. Wu, C. H. Liu, and Z. Zhong, Nano Lett. **10**, 1032 (2010).
[19] D. R. Hines, S. Mezhenny, M. Breban, E. D. Williams, V. W. Ballarotto, G. Esen, A. Southard, and M. S. Fuhrer, Appl. Phys. Lett. **86**, 163101 (2005).
[20] C. Bergenfeldt and P. Samuelsson, Phys. Rev. B **87**, 195427 (2013).
[21] C. Bergenfeldt, P. Samuelsson, B. Sothmann, C. Flindt, and M. Büttiker, Phys. Rev. Lett. **112**, 076803, (2014).
[22] L. D. Contreras-Pulido, C. Emary, T. Brandes, and R. Aguado, New J. Phys. **15**, 095008 (2013).
[23] N. Lambert, C. Flindt, and F. Nori, Europhys. Lett. **103**, 17005 (2013).
[24] J. J. Viennot *et al*. (unpublished).
[25] K. D. Petersson, C. G. Smith, D. Anderson, P. Atkinson, G. A. C. Jones, and D. A. Ritchie, Nano Lett. **10**, 2789 (2010).
[26] A. Cottet, C. Mora, and T. Kontos, Phys. Rev. B **83**, 121311(R) (2011).
[27] A. Cottet, Ph.D. thesis, University Paris VI, 2002.
[28] G. Ithier, E. Collin, P. Joyez, P. J. Meeson, D. Vion, D. Esteve, F. Chiarello, A. Shnirman, Y. Makhlin, J. Schriefl, and G. Schön, Phys. Rev. B **72**, 134519 (2005).
[29] K. D. Petersson, J. R. Petta, H. Lu, and A. C. Gossard, Phys. Rev. Lett. **105**, 246804 (2010).